

Iron oxidation state in lower mantle mineral assemblages

I. Empirical relations derived from high-pressure experiments

C.A. McCammon^{a,*}, S. Lauterbach^{a,b}, F. Seifert^a,
F. Langenhorst^a, P.A. van Aken^b

^a*Bayerisches Geoinstitut, Universität Bayreuth, D-95440 Bayreuth, Germany*

^b*Institut für Mineralogie, Technische Universität Darmstadt, D-64287 Darmstadt, Germany*

Received 2 September 2003; received in revised form 9 January 2004; accepted 16 March 2004

Abstract

The oxidation state of iron can significantly influence the physical and chemical properties of lower mantle minerals. To improve methods for estimation of $\text{Fe}^{3+}/\Sigma\text{Fe}$, synthetic assemblages of $(\text{Mg,Fe})(\text{Si,Al})\text{O}_3$ perovskite and $(\text{Mg,Fe})\text{O}$ ferropericlasite were synthesised from oxide starting mixtures in Re or Fe capsules at 26 GPa and 1650–1850 °C using a multianvil press. $(\text{Mg,Fe})(\text{Si,Al})\text{O}_3$ majorite was also present in some of the run products. Both electron energy loss spectra (EELS) and Mössbauer spectra were measured for each run product, and a robust fitting method was developed for Mössbauer spectra using EELS results as a standard that enabled $\text{Fe}^{3+}/\Sigma\text{Fe}$ of $(\text{Mg,Fe})(\text{Si,Al})\text{O}_3$ perovskite to be determined from Mössbauer spectra of multiphase assemblages. There is a close to linear variation between $\text{Fe}^{3+}/\Sigma\text{Fe}$ and Al concentration in $(\text{Mg,Fe})(\text{Si,Al})\text{O}_3$ perovskite, independent of oxygen fugacity. The concentration of Fe^{3+} in $(\text{Mg,Fe})\text{O}$ increases with increasing iron concentration along curves of constant oxygen fugacity, where higher oxygen fugacity stabilises greater Fe^{3+} concentrations. Fe^{2+}/Mg partition coefficients calculated from chemical composition data corrected for measured $\text{Fe}^{3+}/\Sigma\text{Fe}$ showed values nearly identical within experimental error for all samples, and independent of Al concentration and oxygen fugacity. Simple empirical relations were derived to calculate $\text{Fe}^{3+}/\Sigma\text{Fe}$ in $(\text{Mg,Fe})(\text{Si,Al})\text{O}_3$ perovskite and $(\text{Mg,Fe})\text{O}$ ferropericlasite samples for which no Mössbauer or EELS data were available, and tested by applying them to calculation of Fe^{2+}/Mg partition coefficients from literature data for $(\text{Mg,Fe})(\text{Si,Al})\text{O}_3$ perovskite– $(\text{Mg,Fe})\text{O}$ assemblages where only total iron concentrations had been measured. Results showed Fe^{2+}/Mg partition coefficients that were equal to existing values within experimental error, hence confirming the validity of the empirical relations.

© 2004 Elsevier B.V. All rights reserved.

Keywords: Mössbauer spectroscopy; electron energy loss spectroscopy; ferric iron; cation partitioning; perovskite; ferropericlasite

1. Introduction

The lower mantle constitutes more than half of the Earth by volume; hence physical and chemical properties of lower mantle minerals determine many of the processes that occur within the Earth. Much of our knowledge about the lower mantle has come from experimental studies of mineral assemblages at the

* Corresponding author. Tel.: +49-921-553709; fax: +49-921-553769.

E-mail address: catherine.mccammon@uni-bayreuth.de (C.A. McCammon).

relevant temperature and pressure conditions. Measurements of major, minor and trace element abundance provide information that can be used to infer the properties of the lower mantle. Oxidation state is often neglected due to the difficulties in its measurement, although it is well known that the oxidation state of iron can strongly influence physical and chemical properties of minerals.

The primary phase in the lower mantle, (Mg,Fe)(Si,Al)O₃ perovskite, has been reported to contain large amounts of Fe³⁺ in the presence of Al [1–4], which has been observed to affect properties including elasticity [5], electrical conductivity [6,7] and Fe/Mg partitioning [4,8,9]. The influence of Fe³⁺ on these properties depends both on its concentration and its distribution over crystallographic sites in the crystal structure, and possibly on collateral effects such as vacancy concentration and distribution. Several studies have focused on the concentration of Fe³⁺ in (Mg,Fe)(Si,Al)O₃ perovskite. Lauterbach et al. [2] showed Fe³⁺/ΣFe to be strongly correlated with Al concentration in single-phase assemblages, and essentially independent of oxygen fugacity, while Frost and Langenhorst [4] extended the work to multiphase assemblages, and found a similar correlation with Al concentration. (Mg,Fe)O is also an important lower mantle phase that can incorporate Fe³⁺. At atmospheric pressure it is well known that large amounts of Fe³⁺ can be stable, depending on temperature, oxygen fugacity, and composition, e.g. [10], but at high pressure a phase transformation in the system Fe₃O₄–MgFe₂O₄ significantly reduces the stability of Fe³⁺ in (Mg,Fe)O [11–13].

Investigations of Fe³⁺ concentration in lower mantle assemblages are challenging due to the scarcity of analytical methods that can distinguish the different valence states of iron. Mössbauer spectroscopy has traditionally been used for this task, and has been successful in studies involving only one phase. Such studies are an important first step, but lack the fundamental relevance that multiphase assemblages have for lower mantle phase relations. The calibration of electron energy loss spectroscopy (EELS) for the quantitative determination of Fe³⁺ with high spatial resolution [14] was a significant step that enabled detailed studies of multiphase lower mantle assemblages [4,15]. However, the challenge of sample preparation as well as the beam sensitivity of (Mg,Fe)(Si,Al)O₃ perovskite have

restricted the number of studies (for example, Frost and Langenhorst [4] reported Fe³⁺ values for only 25% of their high-pressure experiments).

There is a strong motivation for deriving an empirical approach to determining Fe³⁺ concentrations in lower mantle minerals. In this study we have applied both Mössbauer spectroscopy and EELS to the quantitative determination of Fe³⁺ concentration in lower mantle assemblages containing (Mg,Fe)(Si,Al)O₃ perovskite and (Mg,Fe)O in order to achieve this goal. We test the usefulness of the empirical relations by applying Fe³⁺ corrections to Fe/Mg partitioning data, and show results that are consistent with the experimental data. The empirical relations therefore provide a realistic approach to Fe³⁺ estimation in samples for which no measurements are available. A second part of this study [16] focuses on a suite of natural samples from the lower mantle (inclusions in diamonds) to compare measured and estimated values of Fe³⁺/ΣFe, and to constrain Fe/Mg equilibrium as well as oxygen fugacity conditions during diamond formation.

2. Experimental methods

Starting materials SL21–23 for the high-pressure experiments were prepared from a mixture of iron powder (not enriched in ⁵⁷Fe) and reagent grade oxides MgO, SiO₂, Al₂O₃ and Fe₂O₃ (95% enriched in ⁵⁷Fe) that were ground together in alcohol and dried in an oven before use. The relative concentration of Fe³⁺ in the starting materials was varied to enable the final oxidation state to be approached from different starting points. B₂O₃ was added to starting material SL23 as a flux to enhance attainment of equilibrium, e.g. [17]. Starting material KLB1 was prepared by R.G. Trønnes from reagent grade oxides and carbonates containing iron unenriched in ⁵⁷Fe, and were ground together in alcohol, decarbonated at 1000 °C in air, then reduced at 1200 °C in a CO₂–CO gas mix furnace at an oxygen fugacity two log units below the fayalite–magnetite–quartz buffer [18]. Mössbauer spectroscopy showed all of the iron in the KLB1 starting material to be Fe²⁺. Chemical compositions of the starting materials are given in Table 1.

High-pressure experiments were performed in a multianvil press with a LaCrO₃ heater assembly and

Table 1
Composition of starting materials and run products

Starting materials (wt.% oxides)															
Run#	SiO ₂	TiO ₂	Al ₂ O ₃	Cr ₂ O ₃	NiO	FeO	Fe ₂ O ₃	MnO	MgO	CaO	Na ₂ O	Σox	Mg#	Fe ³⁺ /ΣFe	
SL21	51.1	–	–	–	–	3.85 ^a	25.82	–	19.3	–	–	96.2	0.75	0.67	
SL22	52.7	–	5.01	–	–	3.96 ^a	18.50	–	19.9	–	–	96.0	0.79	0.58	
SL23	66.0	–	–	–	–	9.57 ^a	–	–	24.4	–	–	90.4	0.82	0.00	
KLB1	44.5	0.16	3.59	0.31	0.25	8.10	–	0.12	39.2	3.44	0.30	99.97	0.90	0.00	
High-pressure run products (cations p.f.u.)															
Run#	phase ^b	Si	Ti	Al	Cr	Ni	Fe ^c	Mn	Mg	Ca	Na	Σcat	Mg#	Fe ³⁺ /ΣFe EELS	Fe ³⁺ /ΣFe Möss
S2069	pv	0.984(20)	–	0.001(1)	–	–	0.108(3)	–	0.923(18)	–	–	2.015(27)	0.895	–	0.32(8)
	fp	0.001(1)	–	0.000(1)	–	–	0.318(3)	–	0.680(14)	–	–	0.999(14)	0.681	–	–
S2104	pv	0.930(19)	–	0.068(2)	–	–	0.158(6)	–	0.879(18)	–	–	2.036(26)	0.848	0.46(10)	0.43(8)
	fp	0.001(1)	–	0.004(1)	–	–	0.378(4)	–	0.614(12)	–	–	0.997(13)	0.618	0.09(5)	–
S2395	pv	0.980(29)	–	0.003(1)	–	–	0.127(11)	–	0.908(27)	–	–	2.019(42)	0.877	0.41(10)	0.38(20)
	fp	0.004(1)	–	0.000(1)	–	–	0.379(8)	–	0.613(18)	–	–	0.996(20)	0.617	0.13(5)	–
S2557	pv	0.932(19)	–	0.068(2)	–	–	0.153(6)	–	0.880(18)	–	–	2.033(26)	0.852	0.48(10)	0.45(20)
	fp	0.001(1)	–	0.003(1)	–	–	0.320(6)	–	0.673(13)	–	–	0.997(15)	0.678	0.00(2)	–
S2671	pv	0.947(28)	–	0.065(2)	–	–	0.125(9)	–	0.884(27)	–	–	2.020(40)	0.876	0.46(10)	0.32(20)
	fp	0.002(1)	–	0.008(1)	–	–	0.363(7)	–	0.621(19)	–	–	0.994(20)	0.631	0.18(10)	–
S2718	pv	0.963(19)	0.003(1)	0.052(2)	0.003(1)	0.001(1)	0.072(3)	0.001(1)	0.897(18)	0.014(1)	0.002(1)	2.008(27)	0.925	–	0.30(20) ^d
	fp	0.003(1)	0.000(1)	0.008(1)	0.004(1)	0.006(1)	0.154(3)	0.001(1)	0.809(16)	0.001(1)	0.012(1)	0.997(17)	0.840	0.03(3)	–
	mj	0.870(17)	0.001(1)	0.259(8)	0.004(1)	0.001(1)	0.064(2)	0.002(1)	0.721(14)	0.067(2)	0.016(1)	2.005(24)	0.918	0.25(5)	–
S2728	pv	0.958(19)	0.004(1)	0.042(1)	0.003(1)	0.000(1)	0.065(6)	0.001(1)	0.921(18)	0.018(1)	0.002(1)	2.016(27)	0.934	–	0.23(20) ^d
	fp	0.001(1)	0.000(1)	0.005(1)	0.003(1)	0.006(1)	0.144(4)	0.001(1)	0.828(17)	0.001(1)	0.009(1)	0.999(17)	0.851	0.02(2)	–
	mj	0.909(27)	0.000(1)	0.220(7)	0.006(1)	0.000(1)	0.057(3)	0.002(1)	0.689(21)	0.083(3)	0.019(1)	1.987(35)	0.923	0.40(10)	–

^a Added as a stoichiometric mixture of metallic Fe and Fe₂O₃.

^b pv: perovskite; fp: ferropericlasite; mj: majorite.

^c Total iron.

^d Determined from relative areas corrected for Fe³⁺ in majorite.

W₇₅Re₂₅/W₉₇Re₃ thermocouple at Bayerisches Geoinstitut. Different oxygen fugacity environments were imposed on the samples through the use of different capsule materials, e.g. [19]: (1) Fe metal (low oxygen fugacity); and (2) Re capsule (higher oxygen fugacity). Although no buffering phase was present, implying that oxygen fugacity probably did not remain constant during the experiment, results from previous experiments suggest that samples synthesised in Fe capsules generally experienced a lower oxygen fugacity compared to samples synthesised in Re capsules [13,20]. Runs using Fe capsules were problematic due to thermocouple contamination and melting of the assembly, but through perseverance we were able to complete successfully one experiment of long duration. Run times were extended to the maximum possible while maintaining temperature stability to optimise chemical homogeneity of the run product. Run conditions are listed in Table 2.

Sample pellets were extracted after high-pressure experiments and prepared for analysis using the electron microprobe, powder X-ray diffraction, Mössbauer spectroscopy and electron energy loss spectroscopy (EELS). Sections were cut from the pellets using a diamond wire saw manufactured by Well (Type 4240) equipped with an 80 µm diamond wire. Powder mounts were prepared by crushing sections in a hydraulic press with hard metal pistons, where both sample and pellet press were precooled using liquid nitrogen. Thin sections were made by grinding and polishing thicker sections to 25–35 µm thickness. For transmission electron microscopy (TEM) investigations the thin sections were mounted on molybdenum grids, and then thinned to perforation with a precision

ion polishing system (PIPS) manufactured by Gatan. No dimpling was performed prior to thinning in order to avoid amorphisation from mechanical stress. As a further measure to reduce amorphisation, we applied the ion beam under a small angle (4°) with a low acceleration voltage in single mode.

X-ray diffraction was used to identify the phases present, and was performed on powder mounts prepared by crushing as described above and then mounting the powder over a 3 mm diameter region on a plastic foil. Chemical compositions were analysed from thin sections using the electron microprobe, and are listed in Table 1. Iron was measured assuming FeO, and then corrected based on the Fe³⁺/ΣFe results from EELS, if available, or Mössbauer spectroscopy.

Electron energy loss spectra were recorded with a Gatan PEELS 666 parallel electron spectrometer attached to a Philips CM20-FEG (field emission gun) transmission electron microscope operating at 200 kV. Operating conditions and procedures have been previously described [2,4]. The Fe³⁺/ΣFe ratios were determined according to methods reported by van Aken et al. [14] and van Aken and Liebscher [21].

Mössbauer spectra were recorded at room temperature (293 K) in transmission mode on a constant acceleration Mössbauer spectrometer with a nominal 1.85 GBq ⁵⁷Co source in a 6 µm Rh matrix (conventional method) or a nominal 370 MBq ⁵⁷Co high specific activity source in a 12 µm Rh matrix (milliprobe method). Further details of the milliprobe method are available in the literature [22,23]. Mössbauer analysis using the conventional method was performed on the same powder mounts used for X-ray diffraction, where absorber thicknesses are estimated to be 1 and 10 mg Fe/cm² for the unenriched and enriched samples, respectively. In several cases (runs S2069 and S2104) it was possible to collect Mössbauer spectra using the milliprobe method on polished sections where phases could be distinguished optically and a piece of Ta foil drilled with a 500 µm diameter hole was used to select the area to be measured. Absorber thicknesses for the thin sections are estimated to be approximately 15 mg Fe/cm². Velocity scales were calibrated relative to 25 µm α-Fe foil using the positions certified for National Bureau of Standards standard reference material no. 1541; line widths of 0.28 mm/s (conventional method) and 0.36 mm/s (milliprobe method) for the outer lines of α-Fe were

Table 2
List of high-pressure experiments

Run	Starting material	<i>P</i> (GPa)	<i>T</i> (°C)	Duration (h)	Capsule	Mineral assemblage ^a
S2069	SL21	26	1700	25	Re	pv, fp
S2104	SL22	26	1750	29	Re	pv, fp
S2395	SL23	26	1700 ^b	4	Re	pv, fp
S2557	SL22	26	1650 ^b	19	Fe	pv, fp, Fe
S2671	SL22	26	1850	10	Re	pv, fp
S2718	KLB1	26	1750	28	Re	pv, fp, mj
S2728	KLB1	26	1850	15	Re	pv, fp, mj

^a pv: perovskite, fp: ferropericlasite, mj: majorite, Fe: Fe metal.

^b Temperature estimated from power curve.

obtained at room temperature. The spectra were fitted to Lorentzian lineshapes using the commercially available fitting program NORMOS written by R.A. Brand (distributed by Wissenschaftliche Elektronik, Germany). Mössbauer spectra took between 1 and 7 days each to collect.

3. Experimental results

Optical examination of thin sections showed all samples to be well crystallised with grain sizes up to 100 μm , where individual phases could be easily identified (Fig. 1a).

Electron microprobe analysis was performed over multiple line profiles with lengths up to 350 μm . The chemical analysis for each phase was determined from averages over the profile, where a minimum of 20 points was used. The degree of homogeneity of the phases can be seen in the standard deviations of cation totals, which include analytical error as well as chemical variation over the profiles (Table 1). The high degree of homogeneity is likely a consequence of the relatively long run times, since shorter run durations produced samples that showed greater compositional variation.

Electron energy loss spectroscopy (EELS) was used as the primary method to measure $\text{Fe}^{3+}/\Sigma\text{Fe}$, since values for individual phases could be unambiguously determined. TEM observations showed that a number of silicate perovskite grains remained crystalline during the sample preparation process, which allowed accurate $\text{Fe}^{3+}/\Sigma\text{Fe}$ measurements to be made (Fig. 1b). $\text{Fe}^{3+}/\Sigma\text{Fe}$ ratios were determined from the white line intensities at the $\text{Fe } L_{23}$ edge according to previous described methods [14,21]. A typical set of spectra for $(\text{Mg,Fe})(\text{Si,Al})\text{O}_3$ perovskite and $(\text{Mg,Fe})\text{O}$ ferropericlasite are illustrated in Fig. 2, and results for all samples that were measured using EELS are listed in Table 1.

Mössbauer spectra could only be collected for the bulk assemblages, and hence show overlapping peaks from all iron-containing phases. To develop a systematic approach to deconvolution, we collected spectra from sample S2069 for three different regions: (1) $(\text{Mg,Fe})(\text{Si,Al})\text{O}_3$ perovskite only; (2) $(\text{Mg,Fe})(\text{Si,Al})\text{O}_3$ perovskite and $(\text{Mg,Fe})\text{O}$ ferropericlasite; and (3) predominantly $(\text{Mg,Fe})\text{O}$ ferropericlasite (Fig.

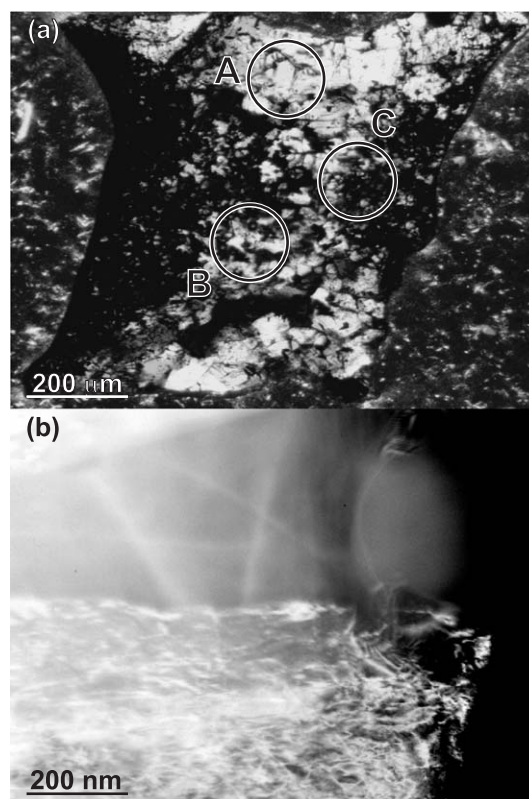


Fig. 1. (a) Optical micrograph (crossed nicols) showing a thin section cut near the centre of the capsule (ca. 0.5 mm diameter) from sample S2069. $(\text{Mg,Fe})(\text{Si,Al})\text{O}_3$ perovskite appears as light regions, while $(\text{Mg,Fe})\text{O}$ ferropericlasite occurs as dark regions. Decompression cracks occurred during quenching and amorphisation occurred along grain boundaries during sample preparation. The three circles indicate the regions over which Mössbauer spectra were recorded. (b) Bright field TEM image of sample S2104 showing the grain boundary between $(\text{Mg,Fe})(\text{Si,Al})\text{O}_3$ perovskite (top) and $(\text{Mg,Fe})\text{O}$ ferropericlasite (bottom).

1a). The spectra are illustrated in Fig. 3. Assuming that $\text{Fe}^{3+}/\Sigma\text{Fe}$ for each phase does not vary in the different regions of the sample, we developed a robust fitting model that minimised the number of variable parameters while maintaining precision within desired limits. For samples consisting exclusively of $(\text{Mg,Fe})(\text{Si,Al})\text{O}_3$ perovskite (pv), four doublets were used to fit the spectra: two $\text{Fe}^{2+}(\text{pv})$, one $\text{Fe}^{3+}(\text{pv})$ and one $\text{Fe}^{n+}(\text{pv})$ [2]. For samples containing moderate amounts of ferropericlasite (fp) (up to ca. 40%), one doublet was added corresponding to $\text{Fe}^{2+}(\text{fp})$, and the weak intensity $\text{Fe}^{n+}(\text{pv})$ doublet was omitted. For samples containing predominantly ferropericlasite, the

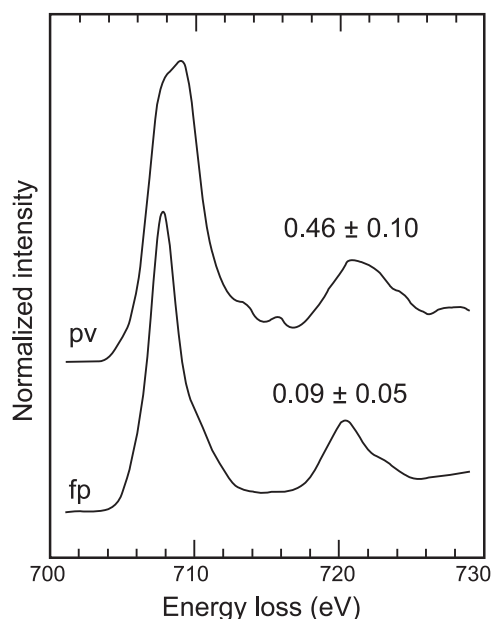


Fig. 2. Background-corrected Fe $L_{2,3}$ -edge electron energy-loss spectra from sample S2104 for $(\text{Mg,Fe})(\text{Si,Al})\text{O}_3$ perovskite (pv) and $(\text{Mg,Fe})\text{O}$ ferropericlasite (fp). $\text{Fe}^{3+}/\Sigma\text{Fe}$ values (indicated above each spectrum) were obtained using data analysis methods previously described [2,14].

second Fe^{2+} (pv) doublet was omitted. For samples containing $(\text{Mg,Fe})(\text{Si,Al})\text{O}_3$ majorite, a doublet was added corresponding to Fe^{2+} (mj). We found that resolution was not sufficient to statistically justify the addition of Fe^{3+} doublets for ferropericlasite or majorite, or a second Fe^{2+} doublet for ferropericlasite.

We calculated the value for $\text{Fe}^{3+}/\Sigma\text{Fe}$ in $(\text{Mg,Fe})(\text{Si,Al})\text{O}_3$ perovskite based on the area ratios of the Fe^{2+} (pv) and Fe^{3+} peaks, corrected for the amount of Fe^{3+} that was found to be present in majorite from EELS data. This correction was necessary because Fe^{3+} doublets from silicate perovskite and majorite have similar hyperfine parameters [2,20]. In contrast, Fe^{3+} in ferropericlasite has a smaller centre shift and quadrupole splitting [11], and hence overlaps with the low-velocity components of both Fe^{2+} and Fe^{3+} in $(\text{Mg,Fe})(\text{Si,Al})\text{O}_3$ perovskite. Since the effect is similar for both Fe^{2+} and Fe^{3+} , there is little effect on $\text{Fe}^{3+}/\Sigma\text{Fe}$. We did not correct $\text{Fe}^{3+}/\Sigma\text{Fe}$ for differing recoil-free fractions [24], since other systematic errors due to the overlapping spectra were estimated to be larger. We estimated uncertainties in $\text{Fe}^{3+}/\Sigma\text{Fe}$ based on statistical errors from the fitting model, as well as

uncertainties in the model itself. Hyperfine parameters are listed in Table 3, and corrected values for $\text{Fe}^{3+}/\Sigma\text{Fe}$ are listed in Table 1.

There is good agreement between $\text{Fe}^{3+}/\Sigma\text{Fe}$ in $(\text{Mg,Fe})(\text{Si,Al})\text{O}_3$ perovskite determined by EELS and by Mössbauer spectroscopy (Table 1). In addition, hyperfine parameters determined from the multiple phase assemblage spectra are in good agreement with

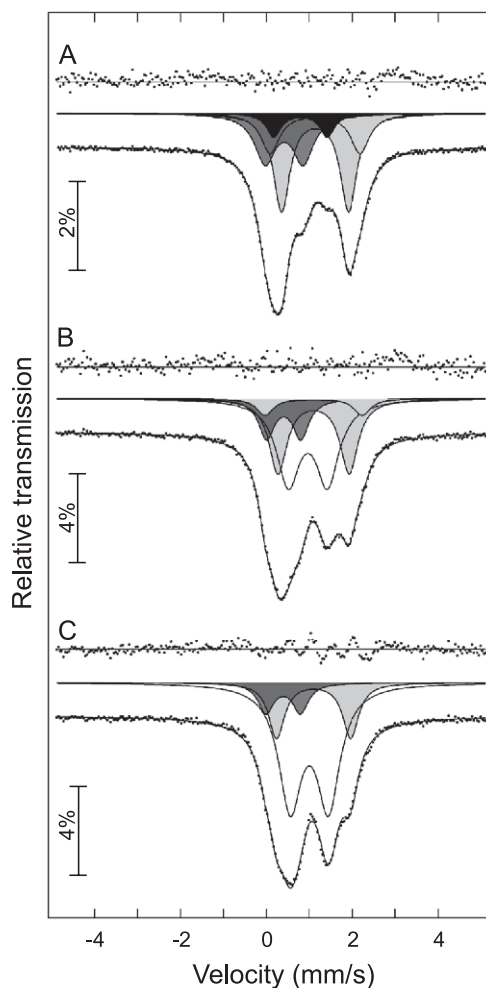


Fig. 3. Room temperature Mössbauer spectra of sample S2069 recorded using a point source (milliprobe method) over the regions indicated in Fig. 1a (100 μm beam diameter). Spectrum A shows $(\text{Mg,Fe})(\text{Si,Al})\text{O}_3$ perovskite (pv) only, while spectra B and C shows varying proportions of $(\text{Mg,Fe})(\text{Si,Al})\text{O}_3$ perovskite (pv) and $(\text{Mg,Fe})\text{O}$ ferropericlasite (fp). Hyperfine parameters are given in Table 3. Subspectra are shaded as follows: Fe^{2+} pv (light grey); Fe^{3+} pv (dark grey); Fe^{n+} pv (black); Fe^{2+} fp (unshaded).

Table 3
Hyperfine parameters derived from room temperature Mössbauer spectra

Run#	S2069 (A)	S2069 (B)	S2069 (C)	S2104	S2395	S2557 ^a	S2671	S2718	S2728
<i>Relative phase areas:</i>									
ferropericlasite (%)		46	68		40	40	44	19	65
majorite (%)								4	12
<i>(Mg,Fe)(Si,Al)O₃ perovskite</i>									
Fe ²⁺ (I)	δ (mm/s)	1.02	0.99	0.99	0.99	0.99	0.98	0.99	0.99
	ΔE_Q (mm/s)	1.56	1.66	1.73	1.52	1.64	1.72	1.73	1.95
	Γ (mm/s)	0.46	0.47	0.45	0.59	0.50	0.52	0.48	0.44
	Relative area (%)	43	32	21	37	23	21	24	53
Fe ²⁺ (II)	δ (mm/s)	1.02	0.99		0.99	0.99	0.98		
	ΔE_Q (mm/s)	2.09	2.26		2.14	2.17	2.38		
	Γ (mm/s)	0.53	0.47		0.48	0.52	0.48		
	Relative area (%)	21	7		16	14	14		
Fe ³⁺	δ (mm/s)	0.30	0.29	0.28	0.28	0.30	0.27	0.32	0.30
	ΔE_Q (mm/s)	0.89	0.80	0.80	0.88	0.94	0.91	0.87	0.91
	Γ (mm/s)	0.59	0.45	0.45	0.44	0.61	0.52	0.48	0.71
	Relative area (%)	27	15	11	39	23	17	18	24
Fe ⁿ⁺	δ (mm/s)	0.68			0.66				
	ΔE_Q (mm/s)	1.25			1.18				
	Γ (mm/s)	0.41			0.37				
	Relative area (%)	9			8				
<i>(Mg,Fe)O ferropericlasite</i>									
Fe ²⁺	δ (mm/s)		0.85	0.89		0.88	0.91	0.90	0.90
	ΔE_Q (mm/s)		0.91	0.89		0.98	1.01	1.00	0.95
	Γ (mm/s)		0.65	0.65		0.77	0.81	0.82	0.47
	Relative area (%)		46	68		40	40	44	19
<i>(Mg,Fe)(Si,Al)O₃ majorite</i>									
Fe ²⁺	δ (mm/s)							1.18	1.18
	ΔE_Q (mm/s)							3.52	3.57
	Γ (mm/s)							0.40	0.40
	Relative area (%)							4	12

Numbers in italics were held fixed during the fitting process.

δ : centre shift (relative to α -Fe); ΔE_Q : quadrupole splitting; Γ : full width at half maximum.

Estimated standard deviations: δ : 0.05 mm/s; ΔE_Q : 0.1 mm/s; Γ : 0.05 mm/s.

^a Also contained Fe metal and magnetically ordered Fe³⁺ (see also [2]).

values reported for individual phases (pv: [2], fp: [11], mj: [20]).

4. Fe³⁺ concentration in (Mg,Fe)(Si,Al)O₃ perovskite

4.1. Al-free (Mg,Fe)SiO₃ perovskite

A dominant influence on Fe³⁺/ΣFe in Al-free (Mg,Fe)SiO₃ perovskite is total iron concentration, where Fe³⁺/ΣFe generally increases with increasing Fe abundance (Fig. 4a). Oxygen fugacity also influences Fe³⁺/ΣFe in Al-free compositions [24]. Sam-

ples synthesised under reducing conditions in Fe capsules (indicated by crosses) have lower Fe³⁺/ΣFe than samples synthesised under more oxidising conditions (Fig. 4a). Also, Fe³⁺/ΣFe in Al-free (Mg,Fe)SiO₃ perovskite appears to be buffered by the degree of silica saturation in the starting material. Initial experiments on Al-free (Mg,Fe)SiO₃ perovskite used silica-saturated starting compositions to inhibit the formation of γ -(Mg,Fe)₂SiO₄ [24], but we chose silica-undersaturated starting compositions in the present work to more accurately represent the bulk composition of the lower mantle. Such behaviour is likely related to the energetics of possible substitution mechanisms [25], and buffering by MgO

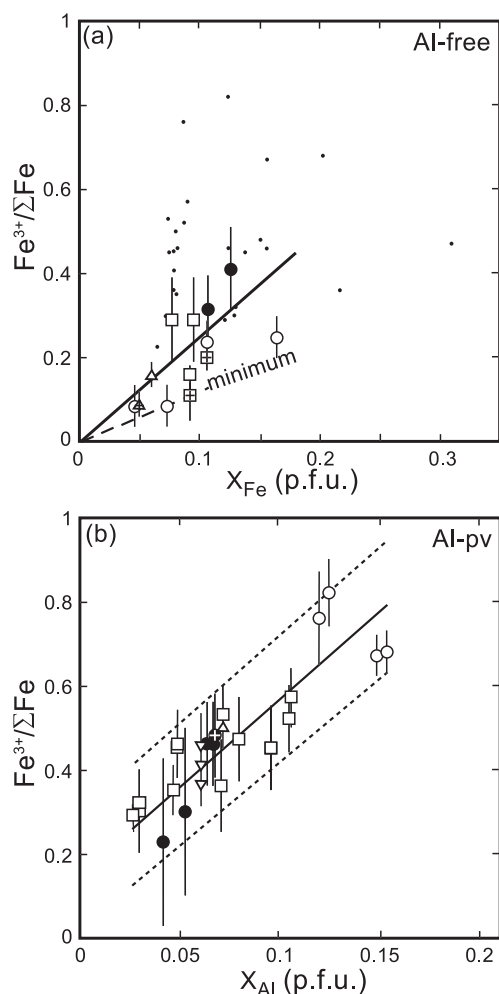


Fig. 4. (a) Relative Fe^{3+} concentration ($\text{Fe}^{3+}/\Sigma\text{Fe}$) versus total iron concentration (in cations per formula unit) in Al-free $(\text{Mg,Fe})\text{SiO}_3$ perovskite (large symbols) and Al-containing $(\text{Mg,Fe})(\text{Si,Al})\text{O}_3$ perovskite (small dots). Symbols are as follows: (a) solid circles (present data); open circles [4]; open squares [2]; open triangles [24]. Crosses indicate experiments carried out using Fe capsules. The solid line indicates a linear fit to all Al-free $(\text{Mg,Fe})\text{SiO}_3$ perovskite data, and the dotted line indicates the estimated minimum $\text{Fe}^{3+}/\Sigma\text{Fe}$ value for a given iron concentration. In Al-containing $(\text{Mg,Fe})(\text{Si,Al})\text{O}_3$ perovskite (small dots) there is little relation between $\text{Fe}^{3+}/\Sigma\text{Fe}$ and iron concentration. (b) Relative Fe^{3+} concentration ($\text{Fe}^{3+}/\Sigma\text{Fe}$) versus Al concentration (in cations per formula unit) in Al-containing $(\text{Mg,Fe})(\text{Si,Al})\text{O}_3$ perovskite. Symbols are as follows: solid circles (present data in Re capsules); solid circle with white cross (present data in Fe capsule); open circles [4]; open squares [2]; open triangle [1]; open inverted triangles [7]. The solid line indicates the best fit to Eq. (1) with 90% prediction limits given by the dashed lines, and is valid for samples synthesised at 24–26 GPa and 1600–1800 °C with $\text{Mg}\# > 0.70$.

instead of SiO_2 can lead to a different equilibrium distribution of defects in silicate perovskite [26].

The data in Fig. 4a provide a basis for assessing the concentration of Fe^{3+} in Al-free $(\text{Mg,Fe})\text{SiO}_3$ perovskite in situations where direct measurements are not available. The dotted line in Fig. 4a gives an indication of the minimum Fe^{3+} concentration at 24–26 GPa and 1600–1800 °C, since syntheses in equilibrium with metallic iron and SiO_2 represent the minimum $f\text{O}_2$ stability limit. The common assumption that all iron is Fe^{2+} will therefore underestimate $\text{Fe}^{3+}/\Sigma\text{Fe}$ by at least 0.1 at the composition $\text{Mg}_{0.9}\text{Fe}_{0.1}\text{SiO}_3$ perovskite, up to a maximum of roughly 0.3 for samples synthesised at higher oxygen fugacity under conditions of silica undersaturation.

4.2. Al-containing $(\text{Mg,Fe})(\text{Si,Al})\text{O}_3$ perovskite

The behaviour of $\text{Fe}^{3+}/\Sigma\text{Fe}$ in Al-containing $(\text{Mg,Fe})(\text{Si,Al})\text{O}_3$ perovskite is significantly different to the behaviour in Al-free compositions. Firstly, total iron concentration is not strongly correlated with $\text{Fe}^{3+}/\Sigma\text{Fe}$ in Al-containing $(\text{Mg,Fe})(\text{Si,Al})\text{O}_3$ perovskite (Fig. 4a). Secondly, the dominant influence on $\text{Fe}^{3+}/\Sigma\text{Fe}$ in $(\text{Mg,Fe})(\text{Si,Al})\text{O}_3$ perovskite is Al concentration (Fig. 4b), consistent with previous work [1,2,4]. Thirdly, Fe^{3+} concentration is invariant with oxygen fugacity in $(\text{Mg,Fe})(\text{Si,Al})\text{O}_3$ perovskite, as demonstrated by the nearly equivalent $\text{Fe}^{3+}/\Sigma\text{Fe}$ values obtained for run S2557 (Fe capsule; solid circle with white cross in Fig. 4a) compared to runs S2104 and S2671 (Re capsules; solid circles in Fig. 4a with nearly identical x_{Al} values) using the same starting material (SL22). As evidence that oxygen fugacity conditions were indeed different, $\text{Fe}^{3+}/\Sigma\text{Fe}$ of co-existing $(\text{Mg,Fe})\text{O}$ was significantly higher for runs S2104 and S2671 (Re capsules) compared to run S2557 (Fe capsule) (see below). Reducing conditions, therefore, lead to an equivalently high $\text{Fe}^{3+}/\Sigma\text{Fe}$ in $(\text{Mg,Fe})(\text{Si,Al})\text{O}_3$ perovskite as for oxidising conditions, which is the same conclusion reached in a previous study [2].

The different behaviour of $\text{Fe}^{3+}/\Sigma\text{Fe}$ in $(\text{Mg,Fe})(\text{Si,Al})\text{O}_3$ perovskite with oxygen fugacity compared to Al-free $(\text{Mg,Fe})\text{SiO}_3$ perovskite, and indeed many other iron-containing minerals, is likely related to the energetics of trivalent cation substitution in silicate perovskite. In Al-free $(\text{Mg,Fe})\text{SiO}_3$ perovskite, reduc-

ing conditions stabilise iron predominantly as Fe^{2+} , and an increase in oxygen fugacity favours the reaction $2\text{FeO} + 1/2 \text{O}_2 = \text{Fe}_2\text{O}_3$ to produce a higher proportion of Fe^{3+} in the perovskite structure. In $(\text{Mg,Fe})(\text{Si,Al})\text{O}_3$ perovskite, the coupled substitution of Fe^{3+} and Al^{3+} into the perovskite structure is energetically favoured, e.g. [25], even under reducing conditions. $\text{Fe}^{3+}/\Sigma\text{Fe}$ is determined primarily by Al concentration, and charge is balanced through disproportionation of Fe^{2+} to Fe^{3+} and Fe metal. An increase in oxygen fugacity enables charge balance through the reaction $2\text{FeO} + 1/2 \text{O}_2 = \text{Fe}_2\text{O}_3$, and the amount of Fe^{2+} disproportionation decreases.

We can construct an analytical expression to predict Fe^{3+} concentration in $(\text{Mg,Fe})(\text{Si,Al})\text{O}_3$ perovskite (Fig. 4b). A linear weighted least-squares fit to all the data gives:

$$\text{Fe}^{3+} / \Sigma\text{Fe} = x_{\text{Fe}^{3+}} / \Sigma x_{\text{Fe}} = 0.15(4) + 4.16(51)x_{\text{Al}}, \quad 0.03 < x_{\text{Al}} < 0.15 \quad (1)$$

where x_i represents the concentration of the i th element in cations per formula unit, and the numbers in parentheses represent standard deviations of the final digits. We fit all available data from the literature, with the exception of values from Litasov et al. [15], which were based on hydrous assemblages. Eq. (1) is valid for samples synthesised at 24–26 GPa and 1600–1800 °C with $\text{Mg}\# > 0.70$.

All data fall within the 90% prediction limits (Fig. 4b), indicating that Eq. (1) provides a more realistic approach to estimating $\text{Fe}^{3+}/\Sigma\text{Fe}$ in the absence of measurements than simply assuming all iron to be Fe^{2+} . Results for natural compositions (data from [1,7], and runs S2718, S2728 from this work) also fall within the 90% prediction limits, where minor elements include Ca, Ti, Cr and Na, in order of decreasing cation abundance. At these abundance levels, the effect of minor elements on $\text{Fe}^{3+}/\Sigma\text{Fe}$ is clearly secondary compared to the influence of Al.

5. Fe^{3+} concentration in $(\text{Mg,Fe})\text{O}$

At ambient pressure it is well established that the Fe^{3+} concentration in $(\text{Mg,Fe})\text{O}$ is determined pri-

marily by temperature and oxygen fugacity, e.g. [10]. The solubility of Fe^{3+} in $(\text{Mg,Fe})\text{O}$ is relatively large at ambient pressure, but decreases at high pressure due to a phase transformation in the system $\text{Fe}_3\text{O}_4\text{--MgFe}_2\text{O}_4$ [11–13]. We calculated the net trivalent cation abundance ($=x_{\text{Fe}^{3+}}+x_{\text{Cr}}+x_{\text{Al}}-x_{\text{Na}}$) from $\text{Fe}^{3+}/\Sigma\text{Fe}$ values and chemical compositions, and the results are plotted in Fig. 5. The main features of the diagram are determined primarily by phase relations in the system $\text{Fe}\text{--}(\text{Mg,Fe})\text{O}\text{--}(\text{Mg,Fe})\text{Fe}_2\text{O}_4$, hence the following discussion focuses on Fe^{3+} only.

The minimum concentration of Fe^{3+} in $(\text{Mg,Fe})\text{O}$ is defined by the phase boundary with metallic iron. At atmospheric pressure there is a moderate amount of Fe^{3+} in $(\text{Mg,Fe})\text{O}$ at equilibrium with metallic iron, particularly for Fe-rich compositions, e.g. [27].

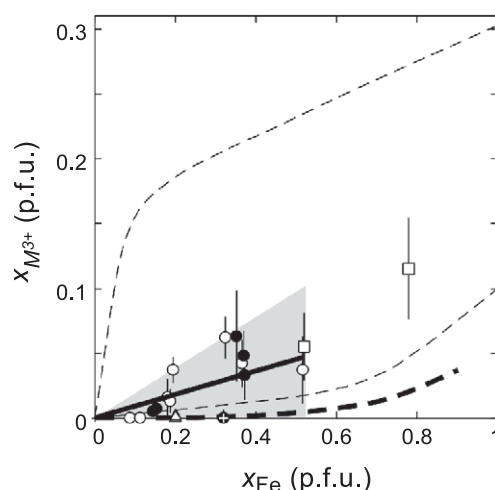


Fig. 5. Net trivalent cation abundance in $(\text{Mg,Fe})\text{O}$ ferropericlasite ($=x_{\text{Fe}^{3+}}+x_{\text{Cr}}+x_{\text{Al}}-x_{\text{Na}}$) versus x_{Fe} , all expressed in cations per formula unit. Symbols are as follows: solid circles (present data in Re capsules); solid circle with white cross (present data in Fe capsule); open circles [4]; open squares [13]; open triangles [11]. The thick dashed line indicates the lower stability limit for Fe^{3+} in $(\text{Mg,Fe})\text{O}$ at 18 GPa and 1400 °C [13], while the stability limits at 1 bar and 1300 °C are from [10] (top thin dashed line) and [27] (bottom thin dashed line). The thick solid line shows the estimated variation of net trivalent cation abundance with iron concentration for runs synthesised at conditions more oxidising than Fe metal equilibrium, where uncertainties are indicated by the grey region. For runs synthesised at reducing conditions in equilibrium with Fe, the Fe^{3+} concentration is close to zero for iron compositions up to approximately 0.5.

At higher pressure, however, the minimum limit decreases, as shown by previous data on ferroperricite–ringwoodite assemblages (1400 °C, 18 GPa) (thick dotted line in Fig. 5) [13]. Results from the present study using a Fe capsule (run S2557; solid circle with white cross in Fig. 5) are in good agreement with this curve.

The maximum concentration of Fe^{3+} in (Mg,Fe)O is defined by the phase boundary with (Mg,Fe) Fe_2O_4 . At atmospheric pressure the maximum amount of Fe^{3+} in (Mg,Fe)O is relatively high [10], and the Re– ReO_2 buffer lies close to the phase boundary [28]. At high pressure, however, the presence of (Mg,Fe)- Fe_2O_4 was reported in (Mg,Fe)O synthesised in Re capsules [13], suggesting that sample compositions were close to the phase boundary. The decrease in the maximum concentration of Fe^{3+} is due to a high-pressure transformation of (Fe,Mg) Fe_2O_4 to a denser phase [11–13], thereby stabilising Fe^{3+} in (Fe,Mg) Fe_2O_4 relative to (Mg,Fe)O.

The data in Fig. 5 provide a basis for assessing the concentration of Fe^{3+} in (Mg,Fe)O in situations where direct measurements are not available. Since $\text{Fe}^{3+}/\Sigma\text{Fe}$ is a function of oxygen fugacity, we have defined two different conditions: (a) Fe capsule (in equilibrium with Fe); and (b) Re capsule (more oxidising than Fe equilibrium). The relations are:

$$\text{Fe} : x_{\text{Fe}^{3+}} = 0.008(4)x_{\text{Fe}}, \quad 0 < x_{\text{Fe}} < 0.5 \quad (2)$$

$$\text{Re} : x_{\text{Fe}^{3+}} = 0.1(1)x_{\text{Fe}}, \quad 0 < x_{\text{Fe}} < 0.5,$$

where all cation compositions are expressed in cations per formula unit. The maximum Fe^{3+} concentration in (Mg,Fe)O for these conditions is approximately at the Re– ReO_2 buffer curve, which is estimated to be:

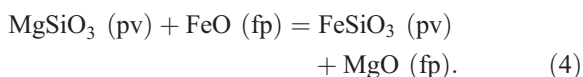
$$\text{Re}/\text{ReO}_2 : x_{\text{Fe}^{3+}} = 0.20(5)x_{\text{Fe}}, \quad 0 < x_{\text{Fe}} < 0.5. \quad (3)$$

The solid line in Fig. 5 indicates the estimated relation for experiments in Re capsules, with uncertainties given by the grey region. For natural compositions the net trivalent cation concentration ($=x_{\text{Fe}^{3+}}+x_{\text{Cr}}+x_{\text{Al}}-x_{\text{Na}}$) should be substituted for $x_{\text{Fe}^{3+}}$.

6. Fe^{2+}/Mg partitioning

Studies of Fe/Mg partitioning between (Mg,Fe)(Si,Al) O_3 perovskite and (Mg,Fe)O provide an ideal dataset for evaluating the usefulness of the empirical equations derived above to estimate Fe^{3+} . These studies have shown that the Fe_{total} concentration of (Mg,Fe)(Si,Al) O_3 perovskite increases relative to (Mg,Fe)O with increasing Al concentration [4,8,9,29–32], which has generally been attributed to the presence of Fe^{3+} . Since we have determined Fe^{2+} and Fe^{3+} individually for each phase in this study, we can use the results to calculate true Fe^{2+}/Mg partition coefficients for our data, and evaluate whether the literature data are consistent with these data after Fe^{3+} corrections have been applied.

The Fe^{2+}/Mg partitioning equilibrium can be expressed according to the following exchange reaction:



The partition coefficient, $K_D = (x_{\text{Fe}}^{\text{pv}} x_{\text{Mg}}^{\text{fp}}) / (x_{\text{Fe}}^{\text{fp}} x_{\text{Mg}}^{\text{pv}})$, expresses the degree to which Fe^{2+} favours the perovskite phase compared to ferroperricite, where the $x_{\text{Fe,Mg}}^{\text{pv,fp}}$ terms are the normalised Fe^{2+} or Mg concentrations in the perovskite or ferroperricite phases, e.g.

$$x_{\text{Fe}^{2+}}^* = x_{\text{Fe}^{2+}} / (x_{\text{Fe}^{2+}} + x_{\text{Mg}}). \quad (5)$$

The results for all experiments where Fe^{3+} was measured directly are plotted in Fig. 6 (solid points), and indicate that $K_D (\text{Fe}^{2+}/\text{Mg})$ is essentially constant over the dataset compared to $K_D (\text{Fe}_{\text{total}}/\text{Mg})$ (small dots). This confirms earlier suggestions that the variation in $K_D (\text{Fe}_{\text{total}}/\text{Mg})$ is primarily due to Fe^{3+} .

The effect of oxygen fugacity on Fe^{2+}/Mg partitioning is negligible. This effect can be seen in the results of the Fe capsule experiment (S2557), where $K_D (\text{Fe}_{\text{total}}/\text{Mg})$ is significantly higher than for the experiments in Re capsules (Table 4). Correction for Fe^{3+} , however, brings the value of $K_D (\text{Fe}^{2+}/\text{Mg})$ in line with other results. This indicates that the decrease observed in $K_D (\text{Fe}_{\text{total}}/\text{Mg})$ as conditions become more oxidising is due to the enhanced stabilisation of Fe^{3+} in (Mg,Fe)O.

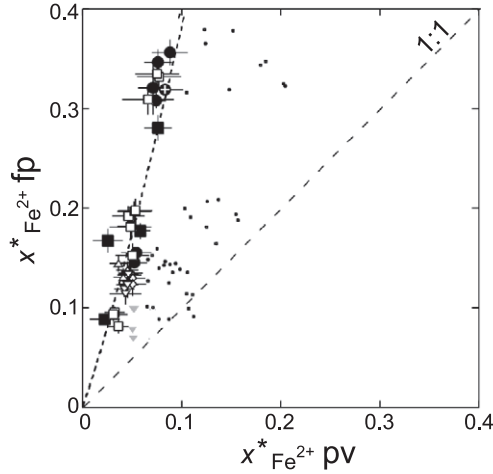


Fig. 6. Fe^{2+} –Mg partitioning between $(\text{Mg,Fe})(\text{Si,Al})\text{O}_3$ perovskite (pv) and $(\text{Mg,Fe})\text{O}$ ferropericlasite (fp). Fe^{2+} concentrations are normalised for each phase to $x_{\text{Fe}^{2+}}^* = x_{\text{Fe}^{2+}} / (x_{\text{Fe}^{2+}} + x_{\text{Mg}})$. Black symbols represent data based on $\text{Fe}^{3+}/\Sigma\text{Fe}$ values determined by either EELS or Mössbauer spectroscopy, while open symbols are based on estimated values. Symbols are as follows: black circles (present data in Re capsules); black circle with white cross (present data in Fe capsule); squares [4]; diamonds [29]; triangles [31]; inverted triangles [32]. The dotted line indicates the best fit of all Fe^{2+} data to Eq. (6), while the dashed line shows the 1:1 correlation. Anomalous low-temperature values [32] (shaded grey) were omitted from the regression. For comparison, normalised Fe_{total} concentrations $[x_{\text{Fe}} / (x_{\text{Fe}} + x_{\text{Mg}})]$ of all data are indicated as small dots.

The Fe^{2+}/Mg partitioning results for the Fe capsule experiment suggests that equilibrium was indeed reached during the run. In contrast, Frost and Langenhorst [4] reported difficulties during experiments using Fe capsules due to the reduction of iron from $(\text{Mg,Fe})\text{O}$ before Fe/Mg equilibrium between $(\text{Mg,Fe})(\text{Si,Al})\text{O}_3$ perovskite and $(\text{Mg,Fe})\text{O}$ was achieved. This is likely related to their starting material, which was a mixture of orthopyroxene and ferropericlasite. The use of mixed oxides in our experiments evidently avoided the problem, where reaction to form equilibrium phases was more rapid than iron precipitation.

In order to calculate K_D (Fe^{2+}/Mg) for the literature data, we estimated Fe^{2+} from total iron concentration in $(\text{Mg,Fe})(\text{Si,Al})\text{O}_3$ perovskite based on Eq. (1), and in $(\text{Mg,Fe})\text{O}$ based on Eq. (2). Even with a relative uncertainty conservatively estimated to be

100%, the small concentration of Fe^{3+} in $(\text{Mg,Fe})\text{O}$ contributes only a small uncertainty to the overall determination of K_D . We omitted previous data [8,9] that have been suggested to lack Fe/Mg equilibrium [4], and corrected K_D for pressure.

The pressure correction for K_D can be determined based on a symmetric regular solution model for both the perovskite and ferropericlasite solid solutions, and assuming that Fe^{2+} and Mg exchange only on the octahedral site of ferropericlasite and the 8–12 coordinated site of perovskite. In this case the equilibrium partitioning of Fe^{2+} and Mg is given by

$$-RT \ln K_D = \Delta G^\circ - W^{\text{pv}}(2x_{\text{Fe}}^{\text{pv}}) + W^{\text{fp}}(2x_{\text{Fe}}^{\text{fp}} - 1). \quad (6)$$

ΔG° is the standard free energy difference of Eq. (4) at the temperature and pressure of interest, W^{pv} and W^{fp} are the symmetric Fe^{2+} –Mg interaction parameters for the perovskite and ferropericlasite solid solutions, respectively, and K_D is the partition coefficient defined above (see [33] for a derivation of Eq. (6)). The pressure dependence of the partition coefficient is given by

$$\frac{\partial \ln K_D}{\partial P} = -\frac{1}{RT} \left[\frac{\partial \Delta G^\circ}{\partial P} - (2x_{\text{Fe}}^{\text{pv}} - 1) \frac{\partial W^{\text{pv}}}{\partial P} \right], \quad (7)$$

where $\partial \Delta G^\circ / \partial P = -\Delta V^\circ$, which is the volume change of reaction (4) at the temperature and pressure of interest. We assumed $\partial W^{\text{fp}} / \partial P = 0$ based on ferropericlasite experimental data [13], and used the value $\partial W^{\text{pv}} / \partial P = 0.11 \text{ kJ mol}^{-1} \text{ GPa}^{-1}$ [34]. The volume change was estimated from experimental data of Fe/Mg partitioning in the Al-free $(\text{Mg,Fe})\text{SiO}_3$ perovskite– $(\text{Mg,Fe})\text{O}$ system [35]. The W^{pv} term is approximately half the magnitude of the ΔG° term, and both contribute to an increase in K_D with increasing pressure. This is in agreement with all experimental studies [30,35,36], as well as crystal chemical analysis that suggests that ΔV° would be negative at all pressures [37]. The effect of pressure on Fe^{2+}/Mg partitioning in the pressure range 21–30 GPa causes an approximately 0.005 GPa^{-1} increase in the value of K_D .

The Fe^{2+}/Mg partitioning results calculated from the literature data are listed in Table 4, and indicate that K_D (Fe^{2+}/Mg) for data where Fe^{3+} was estimated

Table 4

Fe³⁺ concentrations and Fe/Mg partition coefficients for (Mg,Fe)(Si,Al)O₃ perovskite and (Mg,Fe)O

Reference	Sample	P	T	$\text{Fe}^{3+}/\Sigma\text{Fe}$ pv obs	$\text{Fe}^{3+}/\Sigma\text{Fe}$ pv calc	$\text{Fe}^{3+}/\Sigma\text{Fe}$ fp obs	$\text{Fe}^{3+}/\Sigma\text{Fe}$ fp calc	$x_{\text{Fe}^{2+}}^*$ ^a pv	$x_{\text{Fe}^{2+}}^*$ ^a fp	K_D^b $\text{Fe}_{\text{total}}/\text{Mg}$	K_D^c Fe^{2+}/Mg	
This work	2069	26	1700	0.32(8)	— ^d	—	0.10(10)	0.074(9)	0.311(9)	0.25	0.18(2)	
	2104	26	1750	0.46(10)	0.43(11)	0.09(5)	0.09(9)	0.088(16)	0.360(13)	0.29	0.17(3)	
	2395	26	1700	0.41(10)	— ^d	0.13(5)	0.10(10)	0.076(17)	0.350(15)	0.23	0.15(3)	
	2557	26	1650	0.48(10)	0.44(11)	0.00(2)	0.00(1)	0.083(16)	0.322(6)	0.37	0.19(4)	
	2671	26	1850	0.46(10)	0.42(11)	0.18(10)	0.08(8)	0.071(16)	0.324(28)	0.24	0.16(4)	
	2718	26	1750	0.30(20)	0.37(11)	0.03(3)	0.10(10)	0.054(15)	0.156(5)	0.42	0.31(9)	
	2728	26	1850	0.23(20)	0.33(11)	0.02(2)	0.10(10)	0.052(14)	0.146(4)	0.41	0.32(9)	
	[4]	H1495b	25	1650	0.76(11)	0.66(11)	0.00(1)	0.10(10)	0.022(15)	0.088(1)	0.99	0.23(15)
25			1650	0.82(8)	0.68(11)	0.09(8)	0.10(10)	0.025(15)	0.168(12)	0.64	0.12(7)	
25			1650	0.67(5)	0.78(11)	0.07(5)	0.10(10)	0.058(10)	0.178(8)	0.80	0.28(5)	
25			1650	0.68(5)	0.81(11)	0.19(5)	0.10(10)	0.076(14)	0.283(13)	0.52	0.20(4)	
V135b		24	1650		0.53(11)		0.10(10)	0.032(10)	0.095(6)	0.62	0.30(10)	
		24	1650		0.60(11)		0.10(10)	0.044(16)	0.193(10)	0.46	0.19(7)	
		24	1650		0.66(11)		0.10(10)	0.047(17)	0.198(10)	0.54	0.19(7)	
		24	1650		0.67(11)		0.10(10)	0.068(22)	0.335(13)	0.41	0.14(5)	
2705		24	1900		0.61(11)		0.10(10)	0.029(14)	0.093(7)	0.69	0.28(15)	
		24	1900		0.61(11)		0.10(10)	0.046(14)	0.183(9)	0.52	0.21(7)	
		24	1900		0.71(11)		0.10(10)	0.044(17)	0.199(12)	0.60	0.18(7)	
		24	1900		0.70(11)		0.10(10)	0.063(22)	0.338(13)	0.42	0.13(5)	
H1717		25	1900		0.74(11)		0.10(10)	0.039(18)	0.153(12)	0.79	0.22(10)	
		25	1900		0.85(11)		0.10(10)	0.038(28)	0.312(15)	0.53	0.09(7)	
		25	1900		0.57(11)		0.10(10)	0.035(10)	0.081(7)	0.87	0.40(12)	
		25	1900		0.84(11)		0.10(10)	0.028(22)	0.182(13)	0.76	0.13(10)	
[29]		E291	24	1500		0.47(11)		0.12(12)	0.052(12)	0.135(10)	0.61	0.34(9)
		E296	25	1500		0.49(11)		0.11(11)	0.053(13)	0.130(9)	0.67	0.37(9)
[31]	E631	28	1600		0.57(11)		0.12(12)	0.048(14)	0.124(12)	0.75	0.37(11)	
	C133	21	2000		0.45(11)		0.13(13)	0.047(11)	0.138(9)	0.52	0.28(7)	
	C186	21	1800		0.48(11)		0.13(13)	0.038(9)	0.145(8)	0.42	0.21(6)	
[32]	C185	21	1800		0.46(11)		0.12(12)	0.043(10)	0.131(9)	0.51	0.27(7)	
	WC-3	24	1600		0.58(11)		0.15(15)	0.050(16)	0.098(16)	0.98	0.47(18)	
	WC-8	24	1700		0.54(11)		0.16(16)	0.051(22)	0.098(16)	0.91	0.47(23)	
	WC-9	24	1800		0.48(11)		0.14(14)	0.048(12)	0.133(11)	0.57	0.31(8)	
	WC-6	24	1900		0.44(11)		0.13(13)	0.047(10)	0.134(9)	0.53	0.31(7)	
	WC-4	24	2000		0.35(11)		0.14(14)	0.044(10)	0.119(8)	0.49	0.33(8)	
	SD-4	30	1600		0.60(11)		0.21(21)	0.048(17)	0.068(24)	1.25	0.75(34)	
	SD-3	30	1800		0.58(11)		0.22(22)	0.048(13)	0.077(23)	1.09	0.65(25)	
	SD-2	30	2000		0.54(11)		0.16(16)	0.044(11)	0.123(13)	0.64	0.35(9)	
	SD-1	30	2200		0.53(11)		0.13(13)	0.043(16)	0.114(11)	0.67	0.37(13)	

^a Normalised to Fe²⁺/(Fe²⁺ + Mg).^b Based on major element analysis.^c Corrected using measured Fe³⁺/ΣFe for each phase (if available); otherwise using calculated Fe³⁺/ΣFe.^d Not calculated since *x*_{Al} = 0.

are equal within experimental error to values where Fe³⁺ was measured directly. We note in particular that the significant decrease in the Fe_{total}/Mg partition coefficient previously observed with increasing temperature [32] is nearly absent when only Fe²⁺ is considered. As pointed out in [32], the decrease in *K*_D (Fe_{total}/Mg) is accompanied by an increase in

the proportion of majorite, which reduces the concentration of Al in silicate perovskite and hence reduces the amount of Fe³⁺.

We fit the composition data in Table 4 to Eq. (6) using a non-linear weighted least-squares regression. Since the parameters Δ*G*[°], *W*^{pv} and *W*^{fp} are potentially temperature dependent, we divided the data

into three different groups: (1) 1500–1600 °C; (2) 1650–1800 °C; and (3) 1850–2200 °C. Within the data scatter, $RT \ln K_D$ varies with composition in a similar manner for data in all groups, with the exception of the low temperature data from [32], which give significantly smaller values. In contrast, data at the same temperature from [29] show no such reduction. One possibility for the discrepancy could be an equilibration problem at low temperatures in the [32] dataset, although such a suggestion is highly speculative in the absence of further data. For the purpose of the present study, however, we neglected the low temperature data of [32] in the regression.

The parameters in Eq. (6) are highly correlated and best-fit values could not be robustly determined. Instead, we fixed the value of W^{fp} to be 14 kJ/mol according to previous results [27,33,38], and determined the best-fit values for ΔG° and W^{pv} . We found ΔG° to be relatively well constrained (variation between 32.4 and 28.8 kJ/mol) for a large range of W^{pv} values (1 to 5 kJ/mol). We therefore fixed the value of W^{pv} [4], and determined the following best-fit parameters: $\Delta G^\circ = 31.5$ kJ/mol; $W^{\text{pv}} = 2$ kJ/mol; $W^{\text{fp}} = 14$ kJ/mol. We emphasise that these parameters are not unique, but simply represent one model that is consistent with the data.

The fitted curve shows no systematic variation in Fe^{2+}/Mg partitioning between $(\text{Mg,Fe})(\text{Si,Al})\text{O}_3$ perovskite and $(\text{Mg,Fe})\text{O}$ over the conditions and compositions ($T = 1500\text{--}2200$ °C, $P = 21\text{--}30$ GPa and $\text{Mg}\# > 0.75$) represented by the experiments (excluding the anomalous low temperature values [32] discussed above) (Fig. 6). The error bars reflect uncertainties in major element determinations as well as estimations of $\text{Fe}^{3+}/\Sigma\text{Fe}$, where the latter involve relative errors of roughly 25% and 100% for $(\text{Mg,Fe})(\text{Si,Al})\text{O}_3$ perovskite and $(\text{Mg,Fe})\text{O}$, respectively. This allows an assessment of the sensitivity of Fe^{2+}/Mg partition coefficients for temperature, pressure and composition. For example, $\text{Fe}^{3+}/\Sigma\text{Fe}$ in $(\text{Mg,Fe})(\text{Si,Al})\text{O}_3$ perovskite is reported to vary from 45% to 36% with increasing temperature at constant Al concentration [7], yet all $\text{Fe}^{3+}/\Sigma\text{Fe}$ values are within the 90% prediction limits for the linear fit to the data (inverted triangles in Fig. 4). This would produce an increase in K_D for Fe^{2+}/Mg partitioning of only 0.05, which is within our estimated uncertainty. On the other hand,

the neglect of Fe^{3+} altogether leads to more visible effects. Studies at 24 GPa of the assemblage $(\text{Mg,Fe})(\text{Si,Al})\text{O}_3$ perovskite- $(\text{Mg,Fe})(\text{Si,Al})\text{O}_3$ majorite- $(\text{Mg,Fe})\text{O}$ showed that the total iron concentration in $(\text{Mg,Fe})(\text{Si,Al})\text{O}_3$ perovskite decreased significantly between 1800 and 2000 °C, hence decreasing K_D ($\text{Fe}_{\text{total}}/\text{Mg}$) [32]. Correction of total iron concentrations for Fe^{3+} confirms the authors' suggestions that the reduction was due to an increase in the proportion of majorite. K_D (Fe^{2+}/Mg) values at 1800 and 2000 °C vary by only 0.02, compared to a difference in K_D ($\text{Fe}_{\text{total}}/\text{Mg}$) values that is four times larger.

7. Concluding remarks

This study has combined Mössbauer spectroscopy and EELS in order to determine Fe^{3+} concentrations in lower mantle assemblages containing $(\text{Mg,Fe})(\text{Si,Al})\text{O}_3$ perovskite and $(\text{Mg,Fe})\text{O}$, with the goal of constructing empirical relations to estimate Fe^{3+} concentrations in lower mantle phases. We tested the usefulness of the empirical relations by applying Fe^{3+} corrections to Fe/Mg partitioning data in the literature for which no Fe^{3+} measurements had been made, and found good agreement of Fe^{2+}/Mg partition coefficients with experimentally derived values. These empirical relations provide a more realistic basis for estimation of oxidation state in lower mantle minerals than to ignore Fe^{3+} altogether.

Such estimations are important in a wide range of applications. High-pressure studies that include measurements of major and trace element partitioning, melting and phase relations, or incorporation of species such as water would benefit from estimates of Fe^{3+} concentration. For example, the amount of H_2O that can be incorporated into $(\text{Mg,Fe})(\text{Si,Al})\text{O}_3$ perovskite was found to vary with bulk composition, and attributed to different mechanisms of trivalent cation substitution in the perovskite structure [39]. Physical properties such as elasticity and electrical conductivity are known to vary with trivalent cation concentration; for example the threefold increase in conductivity of $(\text{Mg,Fe})(\text{Si,Al})\text{O}_3$ perovskite compared to $(\text{Mg,Fe})\text{SiO}_3$ perovskite is related to the threefold increase in charge carrier abundance, i.e. Fe^{3+} [6]. Estimates of $\text{Fe}^{3+}/\Sigma\text{Fe}$ are also valuable in computer simulations, such as atomistic calculations

to assess trace element partitioning in lower mantle perovskite phases [40]. Other applications include mantle modelling and interpretation of seismic data, particularly in the upper part of the lower mantle where Al concentrations in $(\text{Mg,Fe})(\text{Si,Al})\text{O}_3$ perovskite vary with depth. In addition, trivalent cation concentration is likely to be important in determining physical property differences between MORB and the bulk mantle arising from compositional contrasts.

Acknowledgements

This study was funded by the Deutsche Forschungsgemeinschaft (German Science Foundation) as Projects MC 3/7-1 and 3/7-2 through a PhD student fellowship (SL) and partial support of operating and travel expenses. The work benefited from fruitful discussions with D. Frost and C. Liebske, and the manuscript was significantly improved through a constructive review by B. Harte. [BW]

References

- [1] C.A. McCammon, Perovskite as a possible sink for ferric iron in the lower mantle, *Nature* 387 (1997) 694–696.
- [2] S. Lauterbach, C.A. McCammon, P. van Aken, F. Langenhorst, F. Seifert, Mössbauer and ELNES spectroscopy of $(\text{Mg,Fe})(\text{Si,Al})\text{O}_3$ perovskite: A highly oxidised component of the lower mantle, *Contrib. Mineral. Petrol.* 138 (2000) 17–26.
- [3] A. Gloter, F. Guyot, I. Martinez, C. Colliex, Electron energy-loss spectroscopy of silicate perovskite–magnesiowüstite high-pressure assemblages, *Am. Mineral.* 85 (2000) 1452–1458.
- [4] D.J. Frost, F. Langenhorst, The effect of Al_2O_3 on Fe–Mg partitioning between magnesiowüstite and magnesium silicate perovskite, *Earth Planet. Sci. Lett.* 199 (2002) 227–241.
- [5] D. Andrault, N. Bolfan-Casanova, N. Guignot, Equation of state of lower mantle $(\text{Al,Fe})\text{–MgSiO}_3$ perovskite, *Earth Planet. Sci. Lett.* 193 (2001) 501–508.
- [6] Y. Xu, C.A. McCammon, B.T. Poe, The effect of alumina on the electrical conductivity of silicate perovskite, *Science* 282 (1998) 922–924.
- [7] Y. Xu, C.A. McCammon, Evidence for ionic conductivity in lower mantle $(\text{Mg,Fe})(\text{Si,Al})\text{O}_3$ perovskite, *J. Geophys. Res.* 107 (2002) doi: 10.1029/2001JB000677
- [8] B.J. Wood, D.C. Rubie, The effect of alumina on phase transformations at the 660-kilometer discontinuity from Fe–Mg partitioning experiments, *Science* 273 (1996) 1522–1524.
- [9] B.J. Wood, Phase transformations and partitioning relations in peridotite under lower mantle conditions, *Earth Planet. Sci. Lett.* 174 (2000) 341–354; B.J. Wood, Erratum to: “Phase transformations and partitioning relations in peridotite under lower mantle conditions”, *Earth Planet. Sci. Lett.* 176 (2000) 543.
- [10] D.H. Speidel, Phase equilibria in the system $\text{MgO–FeO–Fe}_2\text{O}_3$: the, 1300 °C isothermal section and extrapolations to other temperatures, *J. Am. Ceram. Soc.* 50 (1967) 243–248.
- [11] C.A. McCammon, J.P. Peyronneau, J.-P. Poirier, Low ferric iron content of $(\text{Mg,Fe})\text{O}$ at high pressures and high temperatures, *Geophys. Res. Lett.* 25 (1998) 1589–1592.
- [12] D. Andrault, N. Bolfan-Casanova, High-pressure phase transformations in the MgFe_2O_4 and $\text{Fe}_2\text{O}_3\text{–MgSiO}_3$ systems, *Phys. Chem. Miner.* 28 (2001) 211–217.
- [13] D.J. Frost, F. Langenhorst, P.A. van Aken, Fe–Mg partitioning between ringwoodite and magnesiowüstite and the effect of pressure, temperature and oxygen fugacity, *Phys. Chem. Miner.* 28 (2001) 455–470.
- [14] P.A. van Aken, B. Liebscher, V.J. Styrsky, Quantitative determination of iron oxidation states in minerals using Fe $L_{2,3}$ -edge electron energy-loss near-edge structure spectroscopy, *Phys. Chem. Miner.* 25 (1998) 323–327.
- [15] K. Litasov, E. Ohtani, F. Langenhorst, H. Yurimoto, T. Kubo, T. Kondo, Water solubility in Mg–perovskites and water storage capacity in the lower mantle, *Earth Planet. Sci. Lett.* 211 (2003) 189–203.
- [16] C.A. McCammon, T. Stachel, J.W. Harris, Iron oxidation state in lower mantle mineral assemblages: II. Inclusions in diamonds from Kankan, Guinea, *Earth Planet. Sci. Lett.*, 222 (2004) 423–434, [this volume](#).
- [17] T. Katsura, E. Ito, Determination of Fe–Mg partitioning between perovskite and magnesiowüstite, *Geophys. Res. Lett.* 23 (1996) 2005–2008.
- [18] R.G. Trønnes, D.J. Frost, Peridotite melting and mineral–melt partitioning of major and minor elements at 22–24.5 GPa, *Earth Planet. Sci. Lett.* 197 (2002) 117–131.
- [19] D.C. Rubie, Characterising the sample environment in multi-anvil high-pressure experiments, *Phase Transit.* 68 (1999) 431–451.
- [20] C.A. McCammon, N.L. Ross, Crystal chemistry of ferric iron in $(\text{Mg,Fe})(\text{Si,Al})\text{O}_3$ majorite with implications for the transition zone, *Phys. Chem. Miner.* 30 (2003) 206–216.
- [21] P.A. van Aken, B. Liebscher, Quantification of ferrous/ferric ratios in minerals: new evaluation schemes of Fe L_{23} electron energy-loss near-edge spectra, *Phys. Chem. Miner.* 29 (2002) 188–200.
- [22] C.A. McCammon, V. Chaskar, G.G. Richards, A technique for spatially resolved Mössbauer spectroscopy applied to quenched metallurgical slags, *Meas. Sci. Technol.* 2 (1991) 657–662.
- [23] C.A. McCammon, A Mössbauer milliprobe: practical considerations, *Hyper. Int.* 92 (1994) 1235–1239.
- [24] C.A. McCammon, The crystal chemistry of ferric iron in $\text{Mg}_{0.95}\text{Fe}_{0.05}\text{SiO}_3$ perovskite as determined by Mössbauer spectroscopy in the temperature range 80–293 K, *Phys. Chem. Miner.* 25 (1998) 292–300.

- [25] N.C. Richmond, J.P. Brodholt, Calculated role of aluminum in the incorporation of ferric iron into magnesium silicate perovskite, *Am. Mineral.* 83 (1998) 947–951.
- [26] A. Navrotsky, A lesson from ceramics, *Science* 284 (1999) 1788–1789.
- [27] I. Srečec, A. Ender, E. Woermann, W. Gans, E. Jacobsson, G. Eriksson, E. Rosén, Activity–composition relations of the magnesiowüstite solid solution series in equilibrium with metallic iron in the temperature range 1050–1400 K, *Phys. Chem. Miner.* 14 (1987) 492–498.
- [28] M.I. Pownceby, H.S.C. O'Neill, Thermodynamic data from redox reactions at high temperatures: IV. Calibration of the Re–ReO₂ oxygen buffer from EMF and NiO + Ni–Pd redox sensor measurements, *Contrib. Mineral. Petrol.* 118 (1994) 130–137.
- [29] T. Irifune, Absence of an aluminous phase in the upper part of the Earth's lower mantle, *Nature* 370 (1994) 131–133.
- [30] D. Andrault, Evaluation of (Mg,Fe) partitioning between silicate perovskite and magnesiowüstite up to 120 GPa and 2300 K, *J. Geophys. Res.* 106 (2001) 2079–2087.
- [31] K. Hirose, Phase transitions in pyrolitic mantle around 670-km depth: Implications for upwelling of plumes from the lower mantle, *J. Geophys. Res.* 107 (2002) doi:10.1029/2001JB000597.
- [32] N. Nishiyama, T. Yagi, Phase relation and mineral chemistry in pyrolite to 2200 °C under the lower mantle pressures and implications for dynamics of mantle plumes, *J. Geophys. Res.* 108 (2003) doi:10.1029/2002JB002216.
- [33] K. Matsuzaka, M. Akaogi, T. Suzuki, T. Suda, Mg–Fe partitioning between silicate spinel and magnesiowüstite at high pressure: experimental determination and calculation of phase relations in the system Mg₂SiO₄–Fe₂SiO₄, *Phys. Chem. Miner.* 27 (2000) 310–319.
- [34] Y. Fei, H.K. Mao, B.O. Mysen, Experimental determination of element partitioning and calculation of phase relations in the MgO–FeO–SiO₂ system at high pressure and high temperature, *J. Geophys. Res.* 96 (1991) 2157–2169.
- [35] F. Guyot, M. Madon, J. Peyronneau, J.P. Poirier, X-ray microanalysis of high-pressure/high-temperature phases synthesized from natural olivine in a diamond anvil cell, *Earth Planet. Sci. Lett.* 90 (1988) 52–64.
- [36] H.K. Mao, G. Shen, R.J. Hemley, Multivariable dependence of Fe–Mg partitioning in the lower mantle, *Science* 278 (1997) 2098–2100.
- [37] S.E. Kesson, J.D. Fitz Gerald, H.S.C. O'Neill, J.M.G. Shelley, Partitioning of iron between magnesian silicate perovskite and magnesiowüstite at about 1 Mbar, *Phys. Earth Planet. Inter.* 131 (2002) 295–310.
- [38] N.M. Wiser, B.J. Wood, Experimental determination of activities in Fe–Mg olivine at 1400 K, *Contrib. Mineral. Petrol.* 108 (1991) 146–153.
- [39] K. Litasov, E. Ohtani, F. Langenhorst, H. Yurimoto, T. Kubo, T. Kondo, Water solubility in Mg-perovskites and water storage capacity in the lower mantle, *Earth Planet. Sci. Lett.* 211 (2003) 189–203.
- [40] A. Corgne, N.L. Allan, B.J. Wood, Atomistic simulations of trace element incorporation into the large site of MgSiO₃ and CaSiO₃ perovskites, *Phys. Earth Planet. Inter.* 139 (2003) 113–127.